https://dx.doi.org/10.1016/j.jcsr.2022.107497

Structural behaviour of Q355 and Q460 press-braked rectangular hollow section stub columns

Haixin Liu[a], Hao Jiang[ab], Yi-Fei Hu[ab*], Tak-Ming Chan[ab], Kwok-Fai Chung[ab]

[a] *Department of Civil and Environmental Engineering, The Hong Kong Polytechnic University, Hong Kong SAR, China*

[b] *Chinese National Engineering Research Centre for Steel Construction (Hong Kong Branch), The Hong Kong Polytechnic University, Hong Kong SAR, China*

(* Corresponding author at: Department of Civil and Environmental Engineering, The Hong Kong Polytechnic University, Hong Kong, China. *E-mail address: yi-fei.hu@polyu.edu.hk*)

Abstract

As inspired by the concept of modular integrated construction, component-assembly-structure, it leads to a great opportunity to reassess the basic structural elements made by an uncommon manufacturing process. Rectangular hollow sections (RHS) can be fabricated by tip-to-tip welding two press-braked channels together to form an integrated cross-section. This unique technique gains more flexibilities and economic efficiencies regarding the setup of production equipment as compared to the mainstream manufacturing process. In this paper, a comprehensive investigation into press-braked RHSs comprising material tests, residual stress measurements, stub column tests, and numerical studies is presented. A total of 40 tensile coupons, 108 sectioned residual stress strips, 10 stub columns, and 290 numerical models were combined to investigate various characteristics of press-braked RHSs. Of the results observed, the strength enhancement of corner materials due to the cold-working can be conservatively captured by the predictive model from AISI S100-16. A simplified predictive residual stress pattern is proposed to represent residual stress distributions of press-braked RHSs. The

applicability of Eurocode 3, ANSI/AISC 360-16, and the direct strength method (DSM) for the design of press-braked RHS stub columns under compression was evaluated based on the experimental and numerical results. And modified design approaches were also proposed and shown to have a more accurate, consistent, and safe prediction of compressive resistance for press-braked RHSs.

Keywords: Cold-formed, Press-braked, Corner strength enhancement, Residual stress, Stub column test, Design.

1. Introduction

Rectangular hollow sections (RHSs, including square hollow sections), are commonly the first choice for engineers when they conceive their structural components. These widely adopted tubular sections possess a simple form of geometry but own extraordinary merits such as outstanding torsional resistance and the possibility to be infilled with concrete to obtain a larger load-bearing capacity. RHS tube products can be generally classified into two sets based on their manufacturing methods, namely hot-finished tubes and cold-formed tubes. Hot-finished RHS tubes may be more favourable because of the uniform distribution of material properties and negligible residual stresses after heat treatment [1]. However, cold-formed RHS tubes still gain their positions in the market due to the merits of comparatively easier fabrication methods and high economic efficiencies. When the RHS tube undergoes cold-working but without post-production heat treatment during their manufacturing process, they can be regarded as cold-formed RHS tubes. There are various cold-working methods to produce cold-formed RHS tubes, including indirect-forming, direct-forming, and tip-to-tip welding of two press-braked channel sections.

For indirect-forming, the steel strip was firstly roll-formed into a circular shape, then the open circular shape was merged by longitudinal welding and subsequently flattened to the desired rectangular hollow section. The magnitude and effect of residual stresses contained in this kind of indirect-formed RHS tube were experimentally and numerically studied by Zhang et al. [2]. Gardner et al. [3] investigated effects of various manufacturing methods on material properties and structural responses on the S355 hot-rolled and S235 cold-rolled RHSs, revealing that the current cross-section slenderness limits may be manufacturing method-dependant based on the compression test results and the plastic design for continuous beam can be equally applied to hot-rolled and cold-rolled RHSs. Research on S500 to S960 cold-rolled RHSs conducted by Wang et al. [4] indicated the partial safety factors of current Eurocode 3 [5] for the design of Class 3 and 4 cross-sections should be greater than unity to yield a required reliability level. Somodi and Kövesdi [6] and Meng and Gardner [7] performed experimental and numerical investigations into the flexural buckling behaviour of cold-rolled high strength RHSs, proposing that a steel grade-dependant imperfection factor α can be incorporated in computing the reduction factor to account for the effects due to different material properties. Moreover, a comprehensive experimental programme on S700 to S1100 cold-rolled RHS structural members was performed by Ma et al. [8-12], and those investigations include material properties, residual stress patterns, stub column tests, beam tests, stub column under compression and bending tests and beam-column tests. Complemented with further parametric studies, corresponding design methods for high strength cold-rolled tubes were subsequently proposed.

With respect to the direct-forming process, the steel strip was directly formed into an open rectangular shape by a set of rollers, and then the opening was closed by the longitudinal welding, typically submerged-arc welding (SAW). The differences in static properties of cold-formed RHSs fabricated by direct-forming and indirect-forming were studied by Sun and Packer [13]. As the section width to plate thickness ratio increases, variations in the full section tensile behaviour between those types of sections are found to become greater. Conversely, the difference in full section compressive behaviour becomes smaller with the increase of the ratio. Galvanized cold-formed steel structures are often applied in bridges, marine structures, and transmission towers because of their superior anti-corrosion ability. Tayyebi et al. [14] and Tayyebi and Sun [15, 16] experimentally investigated the effects of hot-dip galvanizing on the direct-formed RHSs with nominal yield strengths of 355MPa and 690MPa. Post-galvanizing treatment is found to be similar to post-production heat treatment, which can effectively decrease the residual stress level which was introduced during the direct-forming process and greatly delay the initiation of the local buckling, improving the stub column behaviour.

Similar to direct-forming, in which the steel tubes undergo cold-working through a set of coordinated rollers, cold-formed RHS tubes can also be manufactured by tip-to-tip welding of two press-braked channel sections, as shown in Fig. 1. In order to study the effect of fabrication process on the structural behaviour of cold-formed RHS tubes, the combination of press-braking and welding is adopted. It is considered to be more suitable for small-scale production of high strength cold-formed RHS tubes with customized dimensions. As only one press-braking machine is required during the cold-forming process, this method is considered to be simpler and maintains relatively low manufacturing costs. As compared to direct-formed RHSs, press-braked RHSs possess a similar strength enhancement at corner regions and the characteristics of biaxially symmetrical material properties distribution and residual stress pattern, which may lead to some potential benefits when applying this type of RHSs as structural members. As can be found from the previous literature, it is worth noting that the structural behaviours of RHSs are usually manufacturing method-dependant. Press-braked RHSs may exhibit different structural behaviours due to different manufacturing processes. However, investigations on the press-braked RHSs remain rather scarce. Through the increased popularity of modular integrated construction in building construction, it brings the interest to systematically investigate the RHSs made by this type of manufacturing method which adopts a similar assembly concept.

Hence, this paper focuses on studying the various characteristics of press-braked RHSs, comprising (1) Material properties, (2) Residual stress patterns, and (3) Cross-sectional compressive resistances. A comprehensive test programme including tensile coupon tests, residual stress measurements, and stub column tests was performed, while all test specimens were fabricated using the same batch of steel and the same manufacturing method. The objectives of this study are (1) to study structural effects of the manufacturing method on press-braked RHSs, (2) to investigate structural behaviour of stub columns of press-braked RHS under compression, and (3) to evaluate the applicability of current international design approaches for design of press-braked RHSs.

2. Effects of manufacturing method on press-braked RHSs

2.1 General

A total of 8 press-braked RHSs were fabricated using structural steel plates of nominal steel grades Q355 (N series) and Q460 (H series) in this programme. These steel plates were firstly cut into steel strips with v-notches of 30 degrees on both ends for full penetration weld, then the plates were further press-braked to form an open channel section. It is worth noting that the punch radii should be carefully selected to ensure that plastic deformations within the cold-bending corner do not exceed the limitation. EN 10219-2: 2006 [17] also provides recommendations on the ratio of outer corner radius to the tube thickness, which is $2.0 \leqslant R_o/t \leqslant 3.0$ for $6 \text{ mm} < t \leqslant 10$ mm. After press-braking, a careful visual inspection was conducted to check the corner cracking did not occur as the steel plates experienced large plastic deformation. Due to the length limitation of press-braking machines, the total length of specimens is shorter than those fabricated by traditional manufacturing methods. It is more convenient to adopt manual gas-shield metal arc welding when tip-to-tip welding two press-braked channels together, which may introduce unexcepted welding imperfection during manual welding as compared with automatic welding such as the electric resistance welding. To control the quality of welding, the welding parameters were carefully designed to ensure the input linear heat energy does not exceed 1.5kJ/mm. By doing so, the deterioration of mechanical properties around the welding seam can be regarded as have insignificant impact on the structural behaviour of columns. The welding parameters are listed in Table 1 and the definition of dimensions for RHS is shown in Fig. 1.

2.2 Material properties and strength enhancement induced by cold-working

2.2.1 Tensile coupon tests and results

To obtain material properties of the cross-sections under investigation, tensile coupon tests were performed on 8 coupons cut from virgin plates (VP), 16 coupons cut from the flat region of RHS, and 16 coupons extracted from the corner region of the RHSs. The tensile coupons were tested using a 500kN Instron testing system, and the coupon dimensions and test procedure were conformed to the requirements of BS EN ISO 6892-1: 2019 [18]. A pair of strain gauges were affixed to the centre of both sides of the coupon to record the initial axial strains, while 50mm and 25mm extensometers were mounted on the design gauge length of flat and corner coupons respectively to measure the full stress-strain response during the tensile test. Bending residual stresses were released after extracting corner coupons from the specimens, resulting in a slightly curved corner coupon after cutting. Hence, corner coupons were located and tested through a specially designed pin grip. The setups for the tensile tests on flat and corner coupons are shown in Fig. 2.

For each tensile coupon test, the loading strain rate is controlled to follow 3 stages, a strain rate of 0.05%/min is employed from beginning of the test until a yield plateau is observed (or after 0.2% proof strength for corner coupons that have no yield plateau), then a strain rate of 0.1%/min is adopted until the ultimate strength is achieved, and finally a strain rate of 0.2%/min is performed from the ultimate strength to fracture. Stress relaxation for 100 seconds was allowed between each stage to obtain the static material properties. A similar tensile coupon test procedure was also adopted in [19] and [20].

All the test results of the coupons extracted from virgin plates and different locations of the RHSs are tabulated in Tables 2 and 3, where E is Young's modulus of steel, f_y is the yield strength and it is taken as lower yield stress or 0.2% proof stress $f_{0.2\%}$ for the coupons without a yield plateau, f_u denotes the ultimate tensile strength, $\varepsilon_{u,f}$ denotes the corresponding strain at ultimate tensile strength, and ε_f denotes the corresponding strain at fracture, respectively. The following subscripts f and c were designated for distinguishing flat coupons and corner coupons.

The obtained typical full range stress-strain curves of coupons are plotted in Fig. 3. As illustrated in Fig 3, coupons from virgin plates and flat regions exhibit a clearly defined yield point, a yield plateau, and the following strain hardening, while the corner coupons show a more rounded and heavily strength enhanced response, which can be attributed to the cold-working effect induced by press-braking. A good agreement of stress-strain curves is observed between the virgin plates and coupons extracted from the flat region of RHSs, indicating that the manufacturing process does not affect the material properties of flat regions. However, the plastic deformation of the press-braking process results in not only the strength enhancement in corner regions but also a corresponding deterioration of the material's ductility. Unexpected necking was occurred out of the measuring range of the extensometer on some coupons, leading to an incorrectly recorded stress-strain relation after the tensile coupon attained their ultimate tensile strength. To distinguish those coupons, a marker "*" is plotted in the table.

2.2.2 Strength enhancement in corner regions

As can be observed from Tables 2 and 3 and Fig. 3, the material properties of virgin plates and flat regions from the complete section are similar. As compared to the indirect-formed tubes that underwent two-stage plastic deformations, the cross-sections in this study were similar to the direct-formed tubes, since the plastic deformation was only introduced once in corner regions during the whole manufacturing process. An average increase of 43% and 42% in yield strengths of corner regions compared to those in flat regions of RHSs were reported in Table 2-3, respectively. A predictive model for the strength enhancement in the corner region was proposed by Karren [21] and was further adopted in the American specification for the design of cold-formed steel [22], as shown in Eq. (1).

$$\frac{f_{y,c}}{f_{y,f}} = \frac{B_c}{(\frac{r_i}{t})^m} \quad (1)$$

where $B_c = 3.69(f_{u,f}/f_{y,f})-0.819(f_{u,f}/f_{y,f})^2-1.79$, r_i is the inner corner radius of the corner region, taken as the measured outer corner radius r_o minus the plate thickness t, and $m = 0.192(f_{u,f}/f_{y,f})-0.068$.

The results of corner coupon tests in this article are combined with those from press-braked square hollow sections [23-25], press-braked angles [26] and channel sections [27] to evaluate the applicability of Karren's predictive model. A total of extra 49 high strength steel press-braked sections (Measured $f_{y,c}$ > 460MPa) were collated, as shown in Table 4. The measured corner strengths and corresponding predicted corner strengths are plotted in Fig. 4 for comparison. Karren's predictive model is found to provide a conservative prediction for the majority of the data, since the original working range of this model was based on limited test results on normal strength steel. Hence, this predictive model may be extended to high strength steels in a conservative manner. Further systematic test programme on press-braked corners incorporating high strength steel material with various corner radius to thickness ratios shall be conducted to validate and modify the predictive model.

2.3 Residual stress patterns

Residual stress is an important source of material initial imperfection of structural steel members [28]. Due to the presence of residual stresses, part of the material may yield prematurely and that may lead to instability in compression members. A destructive sectioning method was adopted to quantify the magnitude of residual stresses and to determine the residual stress patterns of the cross-sections in the longitudinal direction. 4 typical cross-sections N250×150×6, N250×150×10, H250×150×6, H250×150×10 and one repeated test H250×150×6# were selected and sectioned to investigate their residual stress distribution. As shown in Fig. 5, the cross-sections were all in the length of 300mm and were biaxially symmetrical about the welding seam and axis of symmetry (AOS). Given the biaxially symmetrical geometry, only a quarter of the section was examined for simplicity. A pair of TML general-purpose uniaxial strain gauges with a gauge length of 5 mm were attached to the centre of the strips under the cover of waterproof glues to prevent the containment from the liquid coolant during wire cutting. The membrane residual stresses and bending residual stresses can be computed from the corresponding strain readings on the outer and inner surfaces using Eqs. (2) and (3) [29].

$$\sigma_{\mathrm{m}} = -E\left(\frac{(\varepsilon_{\mathrm{f,out}} - \varepsilon_{\mathrm{i,out}}) + (\varepsilon_{\mathrm{f,in}} - \varepsilon_{\mathrm{i,in}})}{2}\right) \tag{2}$$

$$\sigma_{\mathrm{b}} = \pm E\left(\frac{(\varepsilon_{\mathrm{f,out}} - \varepsilon_{\mathrm{i,out}}) - (\varepsilon_{\mathrm{f,in}} - \varepsilon_{\mathrm{i,in}})}{2}\right) \tag{3}$$

where $\varepsilon_{\mathrm{i,in}}$ and $\varepsilon_{\mathrm{i,out}}$ are the initial strain readings on the inner and the outer surfaces before sectioning, and $\varepsilon_{\mathrm{f,in}}$ and $\varepsilon_{\mathrm{f,out}}$ are the final strain readings after sectioning, respectively.

The converted residual stress distributions of press-braked RHSs, together with a collected residual stress pattern of a square hollow section using the similar manufacturing process [23] are displayed in Fig. 6, in which the positive value of the vertical axis indicates the tensile residual stress. Relatively large tensile membrane residual stresses are discovered in the vicinity of the weld seam, mainly due to the thermal contraction of weld metal after welding. It should be noted that the membrane residual stresses are self-equilibrating within the cross-section. Force equilibriums of membrane residual force within the section are given for each investigated RHSs in Fig. 6, where $F_{\mathrm{m,t}}$ and $F_{\mathrm{m,c}}$ indicate the tensile and the compressive member residual forces, respectively. Bending residual stresses are primarily associated with plastic deformation during the manufacturing process. Those stresses are anticipated to be locked in the RHSs until they have been sectioned. Conforming to the illustrated bending residual stress patterns, most of the steel strips after sectioning remain flat except for the strips located in the corner region, which further confirm that the bending residual stresses mainly exist among the corner regions. Based on the sectioning results and the measured residual stress distributions, a simplified predictive residual stress pattern is subsequently proposed for the press-braked RHSs, as depicted in Fig. 7. It should be noted that the membrane residual stress is independent of the yield strength of steel, while the bending residual stress is related to the yield strength due to plastic deformation, and it fulfils self-equilibrium throughout the thickness of the section.

2.4 Local imperfection measurements

Local imperfection measurements were employed on all stub columns prior to the test. Fig. 8 shows the instrumentation of the local imperfection measurement. The specimen was placed on a milling machine with 3 linear variable displacement transducers (LVDTs, accuracy of 0. 01mm) fixed above. To eliminate the potential imperfection caused by the cold sawing at both ends of the specimen, the measurements were started and finished 50mm away from each end of the specimens. During the measurement, the readings of 3 LVDTs, δ_1, δ_2, and δ_3, were recorded by a data logger, and the local imperfection amplitude δ can be subsequently obtained, while the value δ is equal to $(\delta_1 + \delta_3)/2 - \delta_2$. A typical profile of the measured local imperfection of Section H250×150×6 was shown in Fig. 9. The maximum local imperfection amplitude, δ, measured from each section were also reported in Table 5. It is worth noting that all disclosed geometric defects fulfil the requirements on the tolerance of cold-formed structural hollow sections [17] that the concavity or the convexity of the sides of RHS shall not exceed 0.8%b or 0.8%h.

3. Compressive resistance of press-braked RHS stub columns

3.1 Stub column tests

To investigate the stub column behaviour of press-braked RHSs, fix-ended pure compression tests were performed on 10 stub columns. The stub columns were tested using a 4,600kN MTS compression machine and a 25,000kN POPWILL servo hydraulic testing system, on the basis of the predicted load-bearing capacity of each specimen. Fig. 10 presents the experimental setups for stub column tests for different compression machines. To avoid premature end failure and ensure uniform compression, each end of the stub column was preliminarily milled to be flat before the test and they were restrained by steel rings during the test, and the columns were subsequently positioned between 2 parallel hardened steel plates. A total of 4 strain gauges were mounted at each face of the column at mid-height to record the initial strain history and act as a monitor to adjust the specimen's location during the pre-loading phase. Meanwhile, 2 LVDTs were placed in the diagonal position to measure the axial shortening, Δ. The initial strain readings and obtained axial shortening readings for each specimen were almost the same as their counterparts in the early stage of the compression test, indicating that the stub columns were compressed uniformly during the experiment. The initial strain history was used to modify the early stage of axial load-end shortening curve up to 40% of the measured peak load, eliminating potential effects of any gaps that existed between the specimen and test rig or among the testing machine itself.

The specimens were tested under displacement control with a loading rate of 0.05%×L/min, which was the same as the loading rate employed for the tensile coupon tests. To consistently compare the stub column behaviour with the obtained static material properties, 100s stress relaxation was also conducted when specimens attained their peak loads, to obtain the static ultimate loading-bearing capacities.

3.2 Test results

All tested stub columns exhibited expected local buckling failure modes, as shown in Fig. 11. Once the onset of the local buckling occurred, the bearing-load of columns reached their maximum values and tended to decrease with the development of the local buckling. The key parameters and results of the stub column tests are summarised in Table 5, where b, h, t, r_o are defined in Fig. 1, δ represents the measured maximum local imperfection amplitude, L denotes the specimen length, f_y is the measured yield strength, and N_{Test} denotes the ultimate load-bearing capacity.

The obtained axial loads, N_{Test} are further normalised by the squash loads, Af_y, and they are plotted against the normalized axial shortenings (measured end shortenings divided by the column length, Δ/L) in Fig 12. Clear post-peak trends are observed between different specimens, as the load-bearing capacity of the stockiest cross-section can be maintained for a long plateau, whereas the slenderer cross-section exhibits a rapid deterioration of load-bearing capacity after reaching the peak load. It should be noted that for Sections N250×150×6 and H250×150×6, the repeated test shows a relatively lower load-bearing capacity, and its location of local buckling is more approached to the end of the specimen. It is anticipated that the larger local imperfection (presented in Table 5, δ = 0.29 for Section H250×150×6 and δ = 0.56 for Section H250×150×6#)

may prematurely trigger local plate buckling in such a slender cross-section, directly leading to a reduction in the load-bearing capacity.

3.3 Finite element modelling

In addition to the experimental investigation, finite element modelling on the press-braked RHSs is conducted using commercial software package ABAQUS [30]. The FE modelling aims for replicating the test results on press-braked RHSs and conducting parametric studies to obtain an extended database over a wide range of parameters.

As demonstrated in many studies [9, 31, 32], the structural behaviour of hollow structural steel sections under compression, bending and combined compression and bending can be captured very well by the shell element S4R. On this basis, all FE models on press-braked RHS are established using this 4-node shell element with reduced integration based on the measured material properties, residual stress distributions and geometric dimensions. A mesh convergence study was performed to ensure the accuracy of prediction without losing computational efficiency. When a uniform mesh size of the tube thickness t is employed along the flat region, and three elements are employed for the corner region , the numerical results are found to agree with the test results satisfactorily and can maximise the efficiency simultaneously. The measured material properties of flat and corner coupons from corresponding cross-sections were converted into true stress versus log plastic strain curves before assigning material responses to the flat and corner parts of the column. As part of the flat region near the corner region may be also strengthened due to the cold working effects, the corner material properties were assigned beyond the corner region to the flat region in the prior study to distinguish what level of the strength enhancement in the flat region is.

For press-braked RHSs, their bending residual stresses were directly introduced during the forming process of corners and mainly existed in the corner regions, as illustrated in Fig. 6. However, the effect of bending residual stress is considered to be inherently included in the results of corner coupon tests since the corner coupon was firstly straightened from the state of bend, recovering the bending residual stresses which were released during sectioning. And the membrane residual stresses caused by the thermal contraction arising from the uneven cooling speeds between the molten weld metal and the adjacent parent metal, were explicitly incorporated into the FE models through the ABAQUS 'Initial condition' command to study the effects of membrane residual stress distribution onto the structural behaviour of press-braked RHSs under axial compression. Fig. 13 presents the magnitudes and distributions of the input membrane residual stresses for stub column of Section H250-150-6. For other columns whose residual stress pattern has not been measured, their membrane residual stress distribution was modelled using the predictive model as shown in Fig. 7. To reflect the real boundary conditions during the test, both ends of the column was fully restrained against all degrees of freedom except for the loaded end which allows axial translations. The influence of local geometric imperfections on stub columns were also considered through superposing the lowest elastic buckling mode which was generated from the linear elastic buckling analysis.

3.4 Validation

To evaluate the accuracy of the developed press-braked RHSs FE models, the obtained maximum axial loads and axial load versus end shortening responses from numerical models under various combinations of corner strength enhancement, the existence of residual stresses and amplitudes of local geometric imperfections, were compared with those measured results. As presented in Table 6, the numerical models incorporating corner strength enhancement of 1 times the tube thickness, residual stress distribution and measured local geometric imperfections can well capture the ultimate bearing load during the test. The obtained axial load versus end shortening responses of columns N150-100-6 and H150-100-6 from both experimental and numerical studies are depicted in Fig. 14 for comparison. It can be found that the simulated $N_u - \Delta$ responses yielded satisfactory agreement with those obtained from the experiments. Based on this finding, the effect of membrane residual stresses and the amplitude of local geometric imperfections were further investigated using the developed FE models. The ratios of the numerical results to the experimental results tabulated in Table 6 demonstrate that the existence of membrane residual stresses has a negligible impact on the load-bearing capacity of press-braked RHSs. Though the FE models which only consider the measured imperfection amplitude attain a good agreement with tests, a more accurate prediction of the ultimate loads was achieved by using $0.1t$ as the amplitude of the local geometric imperfections.

3.5 Parametric studies

Upon the verification of the developed FE models, additional parametric studies were performed to supplement the test database over a wider range of cross-sectional sizes. The FE modelling technique adopted in parametric studies were in accordance with those described in

Section 3.4, except for some necessary modifications emphasised herein: (1) the membrane residual stresses were no longer introduced into the modelled columns due to its negligible effect, and (2) the adopted initial local imperfection amplitudes were taken as $0.1t$ for each cross-section. Table 7 summarises the information about geometrical cross-sectional sizes and material properties of all modelled press-braked RHSs, while the column lengths were assigned to be $3h$ for stub columns. In summary, there are 8 types of cross-sections combined with various tube thickness and material properties, resulting in a total of 290 generated numerical results.

4. Assessment and modification of current design methods

4.1 General

Whether a rectangular hollow section can develop its plastic cross-sectional resistance is limited by the onset of local buckling. If the applied load on a cross-section achieves the squash load Af_y before the occurrence of local buckling, this cross-section is deemed as a Class 1-3 (non-slender) section in the design concept of current codes of practice, otherwise, it is classified as a Class 4 (slender) section. Eurocode 3 [33], ANSI/AISC 360-16 [34] and direct strength method (DSM) [22] propose their slenderness limit based on their design concept to account for the local buckling effects of plated structures. However, the current cross-section slenderness limits may be manufacturing method-dependant [3], and all these design methods are based on the test data on hot-finished and cold-rolled steel structural sections. Hence, it is necessary to re-examine their applicability on press-braked RHSs.

4.2 Eurocode 3 and ANSI/AISC 360-16

The current codes of practice Eurocode 3 and ANSI/AISC 360-16 both raise cross-section classification limits and the effective width method for the design of rectangular hollow sections. Classification of a RHS in these codes is dependent on the class of its most slender internal plate element, and this concept treats the entire sections like a collection of separate and independent plated structures. Apparently, this classification method ignores the interaction between plate elements within the cross-section, while an adjacent relative compact plate element was considered to provide a stronger restraint to slenderer plate elements in its vicinity [35]. Hence, as shown in Fig. 15., rectangular hollow sections clearly show a differentiated reduced tendency as compared to square hollow sections, in which the ultimate loads, N_u from both the experimental and the numerical results are normalised by the squash loads, Af_y on the vertical axis and width-to-thickness ratios, c/t are normalised by the parameter $(f_y/E)^{0.5}$ on the horizontal axis. Fitting a linear regression line through the collected SHS data, a fitted classification limit of 1.19 for press-braked RHSs can be figured out between the normalised slenderness limits of Eurocode 3 and ANSI/AISC 360-16.

To compute the reduction in compressive resistance for Class 4 (slender) cross-sections, the effective width method is given that considers the ineffective area of plated structures which suffer from local buckling and do not bear loadings anymore [36]. After excluding the ineffective area of a Class 4 section, the remaining area is regarded as effective enough to develop their plastic resistance, while the effective area A_{eff} can be computed by $A_{eff} = \rho \times A$, in which ρ is the reduction factor and can be calculated according to Eq. (4) from Eurocode 3 and ANSI/AISC 360-16, respectively.

$$\rho_{\mathrm{EWM}} = \begin{cases} 1 & \text{for } \overline{\lambda_{\mathrm{p}}} \le \overline{\lambda_{1}} \\ \left(1 - \mathrm{K} / \overline{\lambda_{\mathrm{p}}}\right) / \overline{\lambda_{\mathrm{p}}} & \text{for } \overline{\lambda_{\mathrm{p}}} > \overline{\lambda_{1}} \end{cases} \tag{4}$$

in which K is 0.22 and 0.2, and $\overline{\lambda_{1}}$ is taken to be 0.673 and 0.724 for Eurocode 3 and ANSI/AISC 360-16, respectively.

To precisely evaluate the design methods and to eliminate the effects of inter-element interaction within rectangular hollow sections, only the results of square hollow sections were extracted [16] and depicted against the plate slenderness with design curves from Eurocode 3 and ANSI/AISC 360-16 in Fig. 16. Current design methods in EC3 and AISC are found to provide unconservative predictions for press-braked RHSs in section classifications as well as compressive resistances. Therefore, the effective width methods from these two codes were modified based on a newly proposed slenderness limit, $c/t = 1.19(f_y/E)^{0.5}$, and it is converted to an equivalent plate slenderness $\overline{\lambda_{\mathrm{p}}}$ = 0.568, as shown in the following equations.

$$\rho_{\mathrm{EWM*}} = \begin{cases} 1 & \text{for } \overline{\lambda_{\mathrm{p}}} \le 0.568 \\ \left(0.899 - 0.187 / \overline{\lambda_{\mathrm{p}}}\right) / \overline{\lambda_{\mathrm{p}}} & \text{for } \overline{\lambda_{\mathrm{p}}} > 0.568 \end{cases} \tag{5}$$

It should be noted that only the cross-sections that were classified as Class 4 (slender) were considered for the evaluation of Eurocode 3, ANSI/AISC 360-16 and the modified effective width method. As presented in Table 8, the N_u/N_{pred} ratios of these design methods were 0.97, 0.95 and 1.02, respectively, indicating that the modified effective width method is able to provide a more safe and accurate prediction for the compressive resistances of press-braked RHS stub columns.

4.3 Direct strength method

The direct strength method was originally proposed for the design of thin-walled cold-formed sections such as angles, channels, and Σ sections, and it is currently adopted in AISI S100-16 [22]. Compared with the effective width method which computes the section resistance based on the *c*/*t* ratio of individual plate elements, DSM regards the whole cross-section as an entirety to consider the inter-element interaction between each plate. Hence, this characteristic makes DSM a more straightforward design method, since it does not involve the complex calculation process of effective areas, effective moduli and shifted centroids. The design formulae of DSM are presented in Eq. (6), in which $\overline{\lambda_{\mathrm{o}}}$ is the overall section slenderness and can be determined from Eq. (7).

$$N_{\mathrm{DSM}} = \begin{cases} Af_{\mathrm{y}} & \text{for } \overline{\lambda_{\mathrm{o}}} \le 0.776 \\ \left[1 - 0.15\left(\dfrac{1}{\overline{\lambda_{\mathrm{o}}}}\right)^{0.8}\right]\left(\dfrac{1}{\overline{\lambda_{\mathrm{o}}}}\right)^{0.8} \times Af_{\mathrm{y}} & \text{for } \overline{\lambda_{\mathrm{o}}} > 0.776 \end{cases} \quad (6)$$

$$\overline{\lambda_{\mathrm{o}}} = \sqrt{\frac{f_{\mathrm{y}}}{f_{\mathrm{cr}}}} \quad (7)$$

According to DSM, the elastic buckling stress f_{cr} of the cross-section is obtained by an elastic buckling analysis using the finite-element analysis software ABAQUS. Therefore, the DSM design curve is consequently obtained and depicted in Fig. 17. DSM also provides rather unconservative predictions for press-braked RHSs not only in the limit between non-slender and slender sections, but also compressive resistances. To further improve the prediction performance of DSM, the original DSM design formulae are modified as Eq. (8) and plotted in Fig. 17, in which the original slenderness limit is taken as 0.677 based on the regression analysis and the design formula in the range of non-slender sections is proposed to provide a better prediction on section resistances.

$$N_{\mathrm{DSM*}}=\begin{cases}1.2\times Af_{\mathrm{y}} & \text{for } \overline{\lambda_{\mathrm{o}}}\le 0.367\\ \left\{2-\left[1-0.204\left(\dfrac{1}{\overline{\lambda_{\mathrm{o,1}}}}\right)^{0.88}\right]\left(\dfrac{1}{\overline{\lambda_{\mathrm{o,1}}}}\right)^{0.88}\right\}\times Af_{\mathrm{y}} & \text{for } \overline{\lambda_{\mathrm{o}}}\le 0.677,\ \overline{\lambda_{\mathrm{o,1}}}=1.354-\overline{\lambda_{\mathrm{o}}}\\ \left[1-0.204\left(\dfrac{1}{\overline{\lambda_{\mathrm{o}}}}\right)^{0.88}\right]\left(\dfrac{1}{\overline{\lambda_{\mathrm{o}}}}\right)^{0.88}\times Af_{\mathrm{y}} & \text{for } \overline{\lambda_{\mathrm{o}}}>0.677\end{cases} \quad (8)$$

The compressive resistance of press-braked RHSs computed using the original and modified DSM design method are normalised to the experimental and numerical results and depicted in Fig. 18. As clearly illustrated in the figure, the proposed modified DSM (DSM*) design method is found to improve the prediction capability of compressive resistances of non-slender sections and provide a more accurate prediction for slender cross-sections. In parallel with the graphical evaluation, quantitative assessment results are presented in Table 8. The corresponding $N_{\mathrm{u}}/N_{\mathrm{pred}}$ ratios of the original and the modified DSM design method are found to be 1.06 and 1.02, with the coefficient of variation being greatly improved from 0.100 to 0.041, indicating that the modified direct strength method offers a more consistent and accurate compressive resistance prediction for press-braked RHS stub columns.

5. Conclusion

A comprehensive test programme is conducted on press-braked Q355 and Q460 rectangular hollow sections to investigate the characteristics of these sections including material properties, residual stress patterns, and cross-sectional compressive resistances. Based on the experimental results and the numerical investigation, conclusions can be drawn as follows:

- Material tests indicate that the flat regions of press-braked RHSs possess a similar unchanged material property of the parent steel plates. Strength enhancements of the corner materials due to one-stage plastic deformation can be conservatively predicted by the AISI S100-16 predictive model.
- Consistent residual stress distributions are found among press-braked RHSs. A simplified predictive residual stress pattern is proposed on the basis of the sectioning results and collected data.
- The stub column tests and the numerical parametric studies reveal that the codified cross-sectional slenderness limits between Class 1-3 (Non-slender) and Class 4 (Slender) sections in Eurocode 3, ANSI/AISC 360-16 and the direct strength method are unconservative. These design methods are modified based on the statistical analysis to offer a better resistance prediction for press-braked RHSs.

Acknowledgements

The authors sincerely acknowledge the support from the Innovation and Technology Fund - Nano and Advanced Materials Institute (ITF-NAMI) for the project "Hong Kong Modular Integrated Construction (MiC) Innovations" (PolyU/ ZS12) and from the Chinese National Engineering Research Centre for Steel Construction (Hong Kong Branch) at The Hong Kong Polytechnic University.

Reference:

[1] X.-Z. Zhang, S. Liu, M.-S. Zhao, S.-P. Chiew, Comparative experimental study of hot-formed, hot-finished and cold-formed rectangular hollow sections, Case Studies in Structural Engineering 6 (2016) 115-129.

[2] X. Zhang, S. Liu, M. Zhao, S.-P. Chiew, Residual stress of cold-formed thick-walled steel rectangular hollow sections, Steel and Composite Structures 22(4) (2016) 837-853.

[3] L. Gardner, N. Saari, F. Wang, Comparative experimental study of hot-rolled and cold-formed rectangular hollow sections, Thin-Walled Structures 48(7) (2010) 495-507.

[4] J. Wang, S. Afshan, N. Schillo, M. Theofanous, M. Feldmann, L. Gardner, Material properties and compressive local buckling response of high strength steel square and rectangular hollow sections, Engineering Structures 130 (2017) 297-315.

[5] CEN, EN 1993-1-1. Eurocode 3: Design of steel structures -Part 1-1: General rules and rules for buildings., European Committee for Standardization, Brussels, 2005.

[6] B. Somodi, B. Kövesdi, Flexural buckling resistance of cold-formed HSS hollow section members, Journal of Constructional Steel Research 128 (2017) 179-192.

[7] X. Meng, L. Gardner, Behavior and Design of Normal-and High-Strength Steel SHS and RHS Columns, Journal of Structural Engineering 146(11) (2020) 04020227.

[8] J.-L. Ma, T.-M. Chan, B. Young, Material properties and residual stresses of cold-formed high strength steel hollow sections, Journal of Constructional Steel Research 109 (2015) 152-165.

[9] J.-L. Ma, T.-M. Chan, B. Young, Experimental investigation on stub-column behavior of

cold-formed high-strength steel tubular sections, Journal of Structural Engineering 142(5) (2016) 04015174.

[10] J.-L. Ma, T.-M. Chan, B. Young, Experimental investigation of cold-formed high strength steel tubular beams, Engineering Structures 126 (2016) 200-209.

[11] J.-L. Ma, T.-M. Chan, B. Young, Cold-Formed High-Strength Steel Rectangular and Square Hollow Sections under Combined Compression and Bending, Journal of Structural Engineering 145(12) (2019).

[12] J.-L. Ma, T.-M. Chan, B. Young, Cold-formed high strength steel tubular beam-columns, Engineering Structures 230 (2021) 111618.

[13] M. Sun, J.A. Packer, Direct-formed and continuous-formed rectangular hollow sections — Comparison of static properties, Journal of Constructional Steel Research 92 (2014) 67-78.

[14] K. Tayyebi, M. Sun, K. Karimi, Residual stresses of heat-treated and hot-dip galvanized RHS cold-formed by different methods, Journal of Constructional Steel Research 169 (2020).

[15] K. Tayyebi, M. Sun, Stub column behaviour of heat-treated and galvanized RHS manufactured by different methods, Journal of Constructional Steel Research 166 (2020).

[16] K. Tayyebi, M. Sun, Design of direct-formed square and rectangular hollow section stub columns, Journal of Constructional Steel Research 178 (2021).

[17] CEN, EN 10219-2: 2006. Cold formed welded structural hollow sections of non-alloy and fine grain steels - Part 2: Tolerances, dimensions and sectional properties., European Committee for Standardization, Brussels, 2006.

[18] BS EN ISO 6892-1-2019. Metallic materials-Tensile testing Part 1: Method for test at room temperature., CEN and BSI (2019).

[19] Y. Huang, B. Young, The art of coupon tests, Journal of Constructional Steel Research 96 (2014) 159-175.

[20] J. Chen, H. Liu, T.-M. Chan, Material properties and residual stresses of cold-formed octagonal hollow sections, Journal of Constructional Steel Research 170 (2020) 106078.

[21] K.W. Karren, Corner properties of cold-formed steel shapes, Journal of the Structural Division 93(1) (1967) 401-432.

[22] AISI, AISI S100-16. North American Specification for the Design of Cold-Formed Steel Structural Members, American Iron and Steel Institute, The United States, 2016.

[23] J.-Y. Zhu, T.-M. Chan, B. Young, Cross-sectional capacity of octagonal tubular steel stub columns under uniaxial compression, Engineering Structures 184 (2019) 480-494.

[24] M. Xiao, Structural behaviour of high strength S690 cold-formed square hollow sections under compression, The Hong Kong Polytechnic University, 2021.

[25] Y. Zhong, Y. Sun, K. Hai Tan, O. Zhao, Testing, modelling and design of high strength concrete-filled high strength steel tube (HCFHST) stub columns under combined compression and bending, Engineering Structures 241 (2021).

[26] L. Zhang, F. Wang, Y. Liang, O. Zhao, Press-braked S690 high strength steel equal-leg angle and plain channel section stub columns: Testing, numerical simulation and design, Engineering Structures 201 (2019).

[27] F. Wang, O. Zhao, B. Young, Testing and numerical modelling of S960 ultra-high strength steel angle and channel section stub columns, Engineering Structures 204 (2020).

[28] M. Xiao, Y.-F. Hu, H. Jin, K.-F. Chung, D.A. Nethercot, Prediction of residual stresses in high-strength S690 cold-formed square hollow sections using integrated numerical simulations,

Engineering Structures 253 (2022).

[29] R.B. Cruise, L. Gardner, Residual stress analysis of structural stainless steel sections, Journal of Constructional Steel Research 64(3) (2008) 352-366.

[30] ABAQUS, Dassault Systems, Waltham, MA, USA (2019).

[31] X. Yun, Z. Wang, L. Gardner, Structural performance and design of hot-rolled steel SHS and RHS under combined axial compression and bending, Structures 27 (2020) 1289-1298.

[32] H.-X. Liu, H. Fang, J.-Y. Zhu, T.-M. Chan, Numerical investigation on the structural performance of octagonal hollow section columns, Structures 34 (2021) 3257-3267.

[33] prEN 1993-1-1:2020. Eurocode 3: Design of steel structures -Part 1-1: General rules and rules for buildings, European Committee for Standardization (CEN) Brussels (2020).

[34] AISC/AISC, ANSI/AISC 360-16. Specification for structural steel buildings, American Institute of Steel Construction, Chicago, 2016.

[35] R. Gonçalves, D. Camotim, Elastic buckling of uniformly compressed thin-walled regular polygonal tubes, Thin-Walled Structures 71 (2013) 35-45.

[36] CEN, EN 1993-1-5. Eurocode 3 — Design of steel structures — Part 1-5: Plated structural elements., European Committee for Standardization, Brussels, 2006.

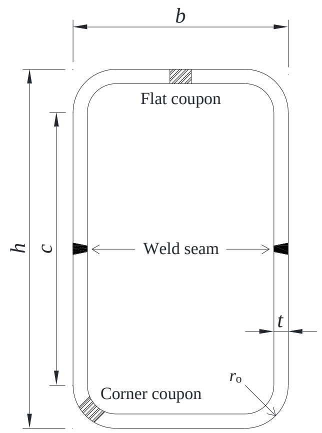

Fig. 1. Definition of dimensions for the press-braked RHS.

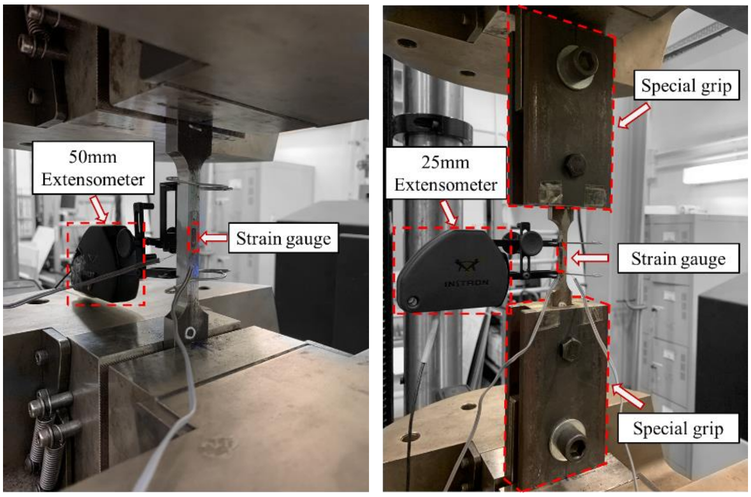

(a) Flat coupon.
(b) Corner coupon.

Fig. 2. Test setup for tensile coupon tests.

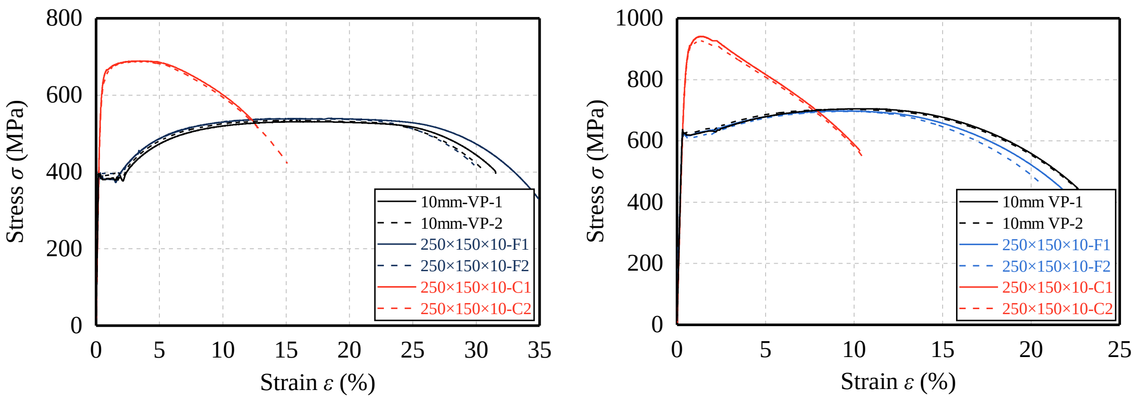

(a) N250×150×10.
(b) H250×150×10.

Fig. 3. Typical stress-strain curves obtained from coupon tests.

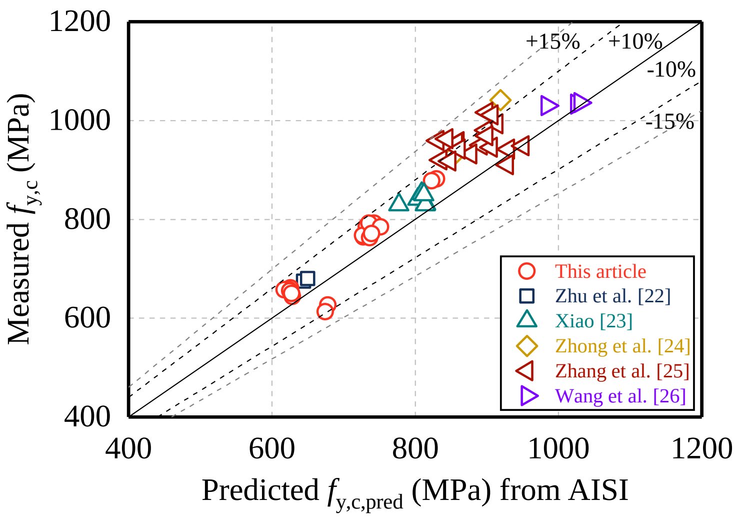

Fig. 4. Comparisons between measured and predicted yield strengths of corner materials.

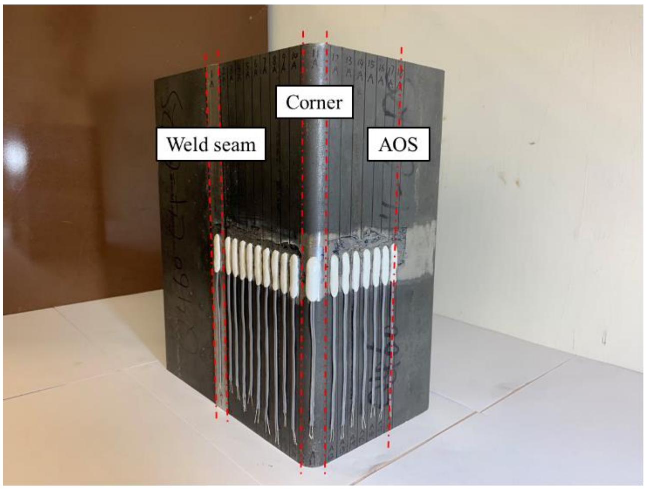

(a) Before sectioning.

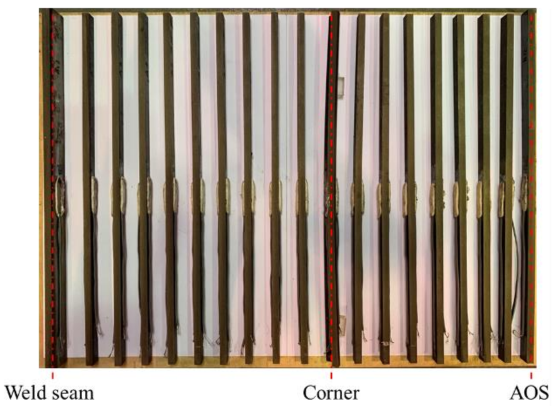

(b) After sectioning.

Fig. 5. Sectioning of press-braked RHS H250×150×6.

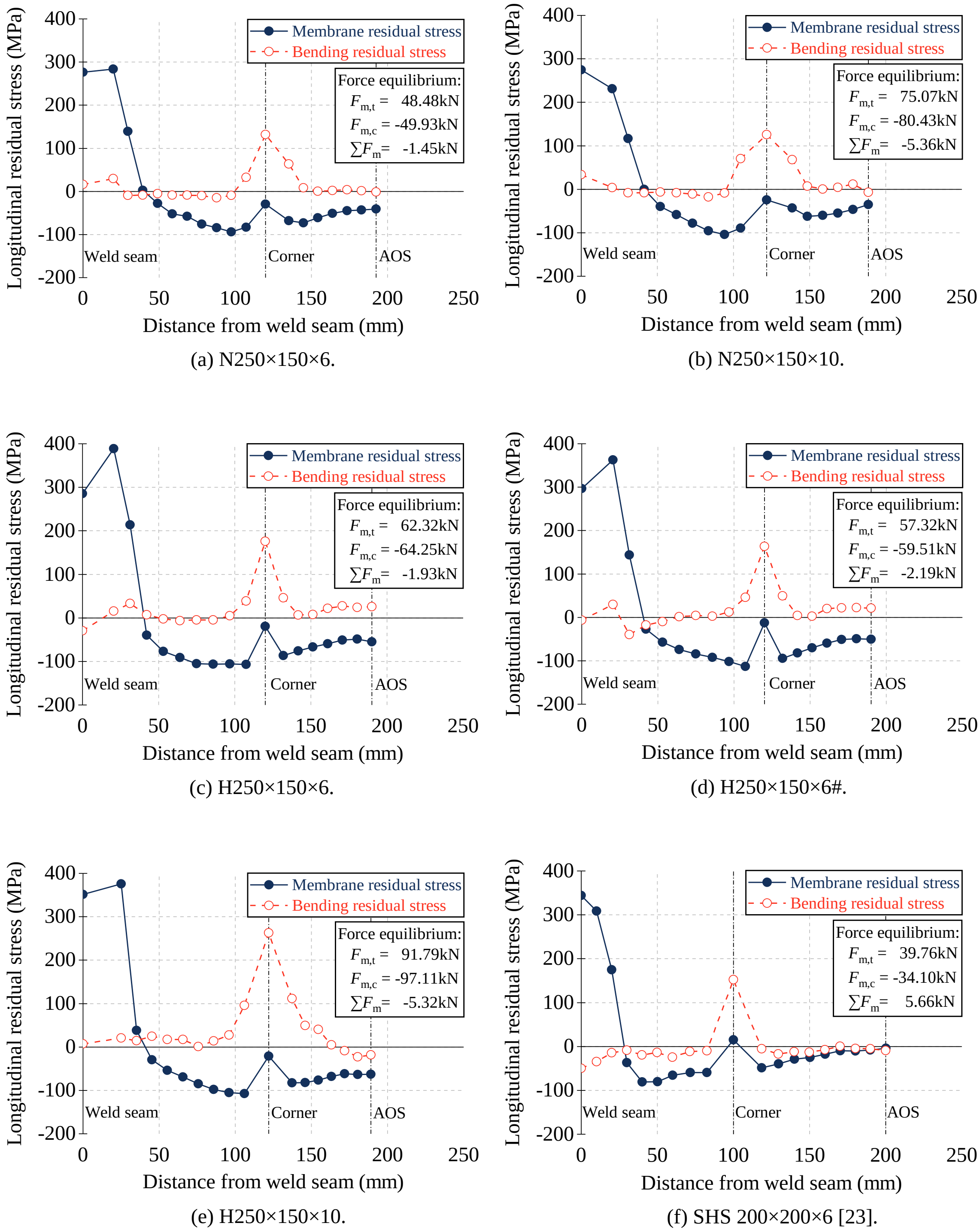

Fig. 6. Residual stress distributions of press-braked RHSs.

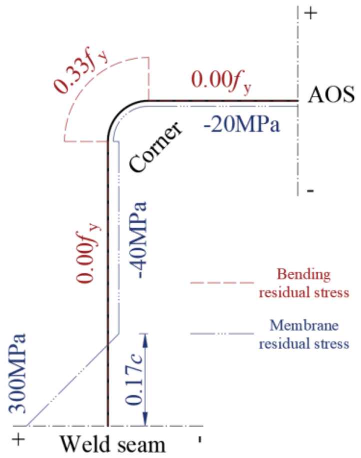

Fig. 7. The simplified predictive residual stress pattern of press-braked RHS.

Fig. 8. Instrumentation of the local imperfection measurement.

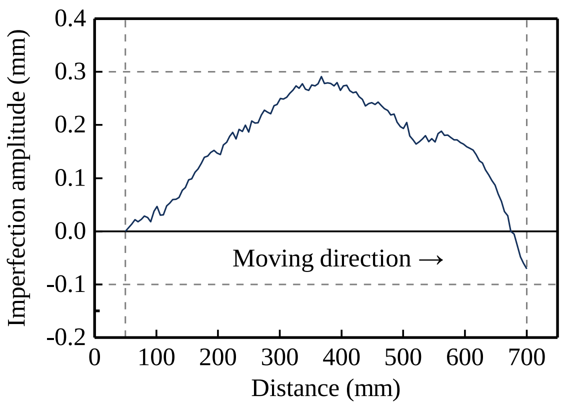

Fig. 9. The local imperfection profile of specimen H250×150×6.

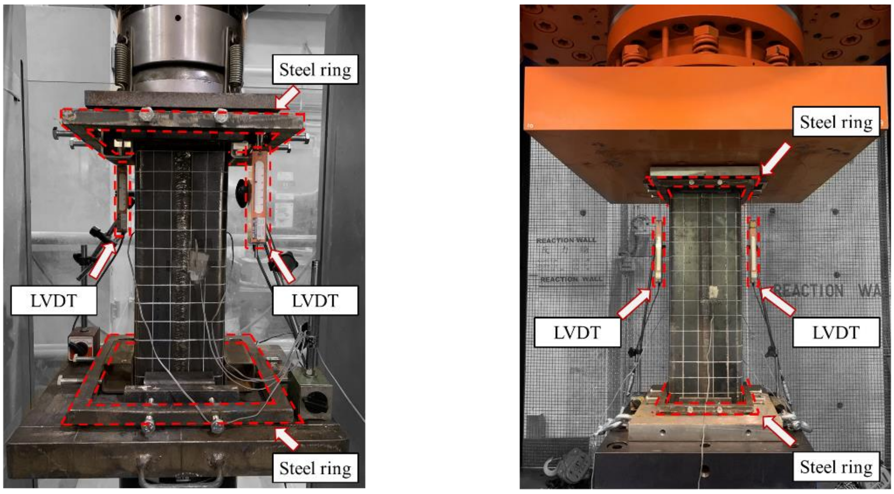

(a) 4600kN MTS hydraulic compression machine. (b) 25000kN Popwill universal compression machine.

Fig. 10. Stub column test setups.

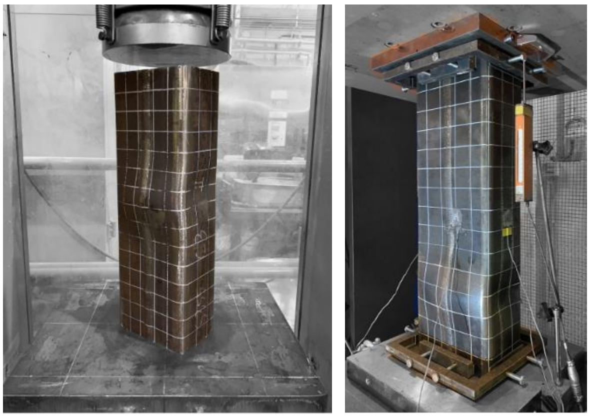

(a) N120×80×6. (b) H250×150×10.

Fig. 11. Typical failure modes of press-braked RHS stub columns.

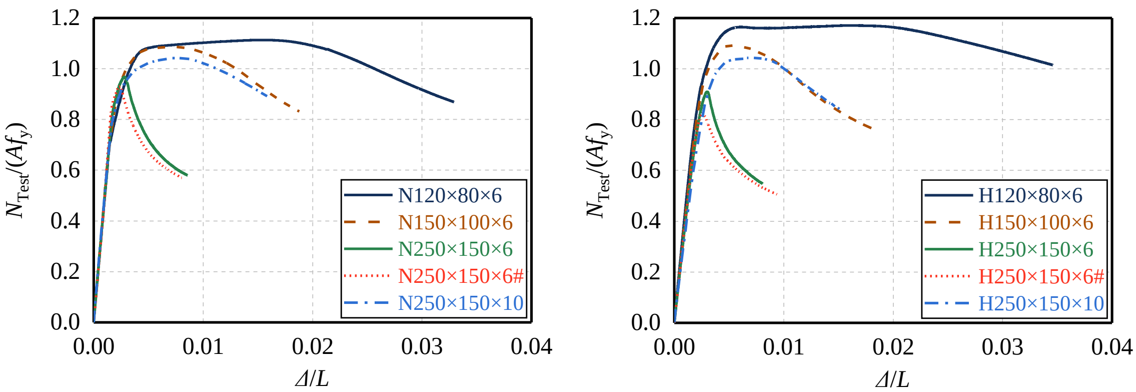

(a) N series. (b) H series.

Fig. 12. Normalised axial strength versus axial strain curves of press-braked RHS stub columns.

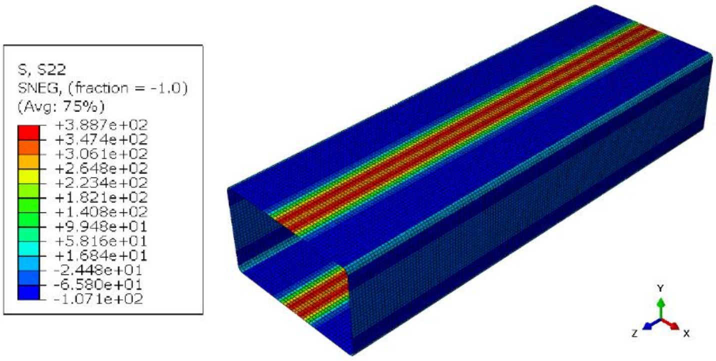

Fig. 13. Input membrane residual stress distribution for H250×150×6 FE model.

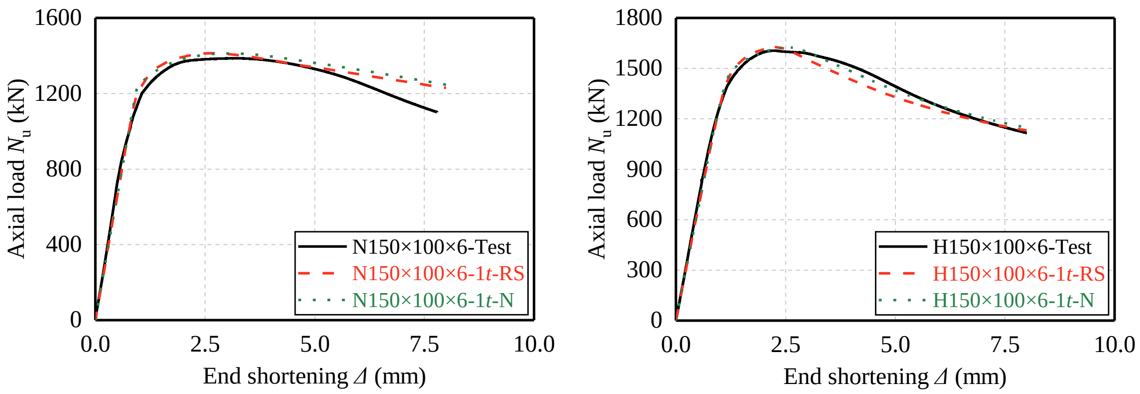

(a) N150×100×6. (b) H150×100×6.

Fig. 14. Comparisons of axial load versus end shortening curves between experimental and numerical results.

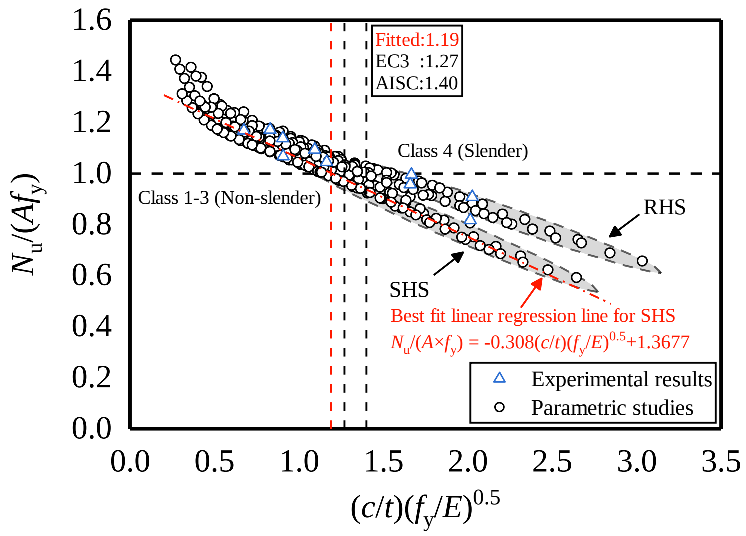

Fig. 15. Evaluation of the cross-section classification for press-braked RHSs.

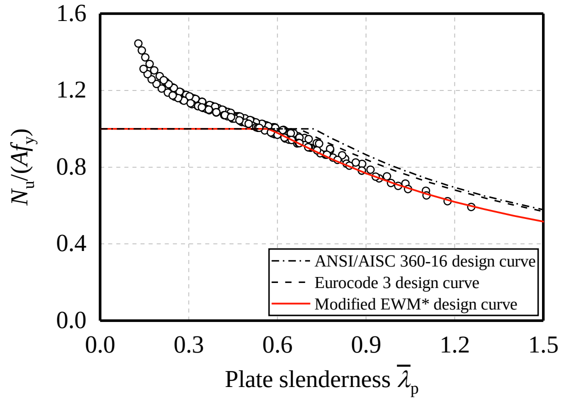

Fig. 16. Comparison of test and FE results with effective width method-based design approaches.

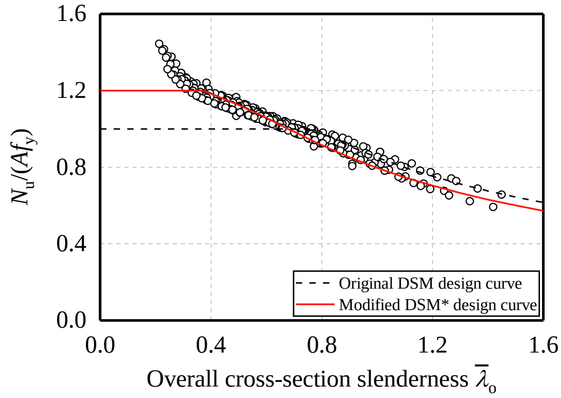

Fig. 17. Comparison of test and FE results with original and modified direct strength methods.

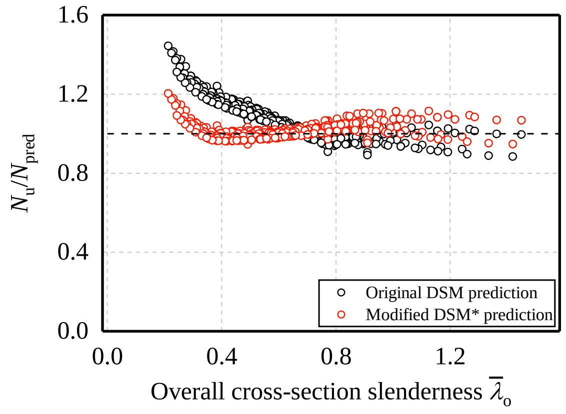

Fig. 18. Comparison of test and FE results normalized by original and modified direct strength methods.

Table 1. Welding parameters for the Gas-shield metal arc welding.

Nominal steel grade	Thickness	Voltage	Current	Welding speed	Line heat input
-	mm	V	A	mm/min	kJ/mm
Q355	6	24	210	200	1.21
Q355	10	30	260	240	1.56
Q460	6	24	210	200	1.21
Q460	10	30	260	240	1.56

Table 2. Measured material properties of N series press-braked RHSs.

Section	Flat coupons					Corner coupons				
	E	$f_{y,f}$	$f_{u,f}$	$\varepsilon_{u,f}$	$\varepsilon_{f,f}$	E	$f_{y,c}$	$f_{u,c}$	$\varepsilon_{u,c}$	$\varepsilon_{f,c}$
-	GPa	MPa	MPa	%	%	GPa	MPa	MPa	%	%
N6mm-VP	210	438	529	15.63	29.51	-	-	-	-	-
	209	440	533	14.44	30.67	-	-	-	-	-
N120×80×6	215	431	527	14.99	28.46	215	661	713	2.93	13.10
	212	433	526	14.32	28.74	213	657	710	2.98	13.66
N150×100×6	212	433	521	15.21	28.92	215	657	709	2.47	12.37
	211	431	526	14.48	27.71	211	655	707	2.19	11.08
N250×150×6	209	435	530	14.97	31.97	201	644	697	2.22	12.96
	212	429	527	15.85	30.76	198	650	705	1.90	11.48
N10mm-VP	213	383	531	16.99	31.54	-	-	-	-	-
	214	392	534	17.11	31.05	-	-	-	-	-
N250×150×10	202	381	540	18.36	34.91	200	626	689	3.47	12.73
	214	397	539	15.35	30.10	195	613	688	3.49	15.11

Table 3. Measured material properties of H series press-braked RHSs.

Section	Flat coupons					Corner coupons				
	E	$f_{y,f}$	$f_{u,f}$	$\varepsilon_{u,f}$	$\varepsilon_{f,f}$	E	$f_{y,c}$	$f_{u,c}$	$\varepsilon_{u,c}$	$\varepsilon_{f,c}$
-	GPa	MPa	MPa	%	%	GPa	MPa	MPa	%	%
H6mm-VP	201	520	597	12.73	24.24	-	-	-	-	-
	206	533	615	13.34	24.76	-	-	-	-	-
H120×80×6	212	529	604	12.74	24.18	207	767	799	1.81	4.68*
	212	523	607	13.45	18.19*	207	763	792	1.88	8.74*
H150×100×6	209	542	618	11.72	22.67	212	792	834	1.86	5.56*
	211	540	613	12.59	25.86	209	792	832	1.76	8.12*
H250×150×6	217	565	632	11.67	22.13	213	784	822	1.11	12.56
	217	554	621	12.05	25.04	216	771	822	1.60	4.71*
H10mm-VP	215	622	705	10.58	22.70	-	-	-	-	-
	218	628	704	9.47	22.59	-	-	-	-	-
H250×150×10	215	617	698	9.27	22.31	217	882	941	1.37	10.34
	215	623	697	9.59	20.62	211	878	926	1.35	10.47

Note: * denotes for the coupon whose necking occurred out of the measuring range.

Table 4. Collection of literature on press-braked sections: Material properties and geometrics.

References	$f_{y,f}$	$f_{y,c}$	t	R_i	Predicted/Measured
-	MPa	MPa	mm	-	-
This article	381-628	613-882	5.74-9.72	0.91-1.20	0.91-1.08
Zhu et al. [22]	476-478	675-680	5.94-5.96	1.51-1.52	1.04-1.05
Xiao [23]	783-796	830-852	5.86-5.89	3.04-3.06	1.02-1.07
Zhong et al. [24]	718-762	927-1041	4.96-5.93	1.44-1.51	1.09-1.13
Zhang et al. [25]	635-764	910-1016	4.25-4.98	1.50-1.74	0.98-1.15
Wang et al. [26]	928-966	1030-1036	6.01-6.11	2.45-2.48	1.01-1.05

Table 5. Key parameters and results of press-braked RHS stub column tests.

Specimen	b	h	t	r_o	δ	L	Af_y	N_{Test}	N_{Test}/Af_y
-	mm	mm	mm	mm	mm	mm	kN	kN	-
N120×80×6	80.34	119.83	6.18	14.0	0.13	360	1036	1153	1.11
N150×100×6	99.30	149.28	6.12	13.5	0.39	445	1276	1386	1.09
N250×150×6	149.55	249.28	6.05	13.5	0.65	748	2050	1983	0.97
N250×150×6#	149.80	249.75	6.09	13.5	1.14	750	2066	1921	0.93
N250×150×10	149.06	249.55	9.79	21.5	0.21	749	2946	3071	1.04
H120×80×6	79.91	119.02	5.85	11.0	0.24	360	1110	1300	1.17
H150×100×6	99.70	149.29	5.90	11.0	0.26	445	1470	1605	1.09
H250×150×6	148.62	249.98	5.81	11.0	0.29	748	2467	2244	0.91
H250×150×6#	149.54	249.60	5.80	10.5	0.56	749	2471	2042	0.83
H250×150×10	148.62	249.80	9.89	19.0	1.10	750	4494	4694	1.04

Note: # denotes for the repeated test.

Table 6. Comparisons of test results to different FE models.

Specimen	N_{FE}/N_{Test}						
	Incorporate residual stress			Without residual stress			
-	0*t*-RS	1*t*-RS	2*t*-RS	1*t*-N-Measured	1*t*-N-0.05*t*	1*t*-N-0.10*t*	1*t*-N-0.15*t*
N120×80×6	0.99	1.06	1.13	1.06	1.04	1.01	1.00
N150×100×6	0.97	1.02	1.07	1.02	1.02	1.00	0.98
N250×150×6	0.94	0.96	0.98	0.97	1.00	0.97	0.96
N250×150×6#	0.93	0.95	0.97	0.97	1.04	1.00	0.99
N250×150×10	1.02	1.09	1.17	1.09	1.07	1.04	1.02
H120×80×6	0.92	0.98	1.04	0.98	0.98	0.96	0.95
H150×100×6	0.97	1.01	1.06	1.01	1.01	0.98	0.97
H250×150×6	0.96	0.97	0.98	0.98	0.98	0.96	0.94
H250×150×6#	0.97	0.99	1.00	1.01	1.08	1.06	1.04
H250×150×10	0.98	1.03	1.08	1.03	1.06	1.03	1.01
Mean:	0.96	1.01	1.05	1.01	1.03	1.00	0.98
COV:	0.030	0.045	0.064	0.039	0.034	0.033	0.032

Table 7. Adopted parameters in parametric studies.

Cross-section type	Dimension	Thickness	R_o	Yield strength	Nos
-	mm	mm	mm	MPa	-
RHS	80-120, 100-150, 120-200, 150-250	4-10	2*t*	433-565	146
SHS	100-100, 140-140, 180-180, 220-220	4-10	2*t*	433-565	144

Table 8. Comparisons between test and FEM results and design methods.

Specimens	Nos	N_u/N_{EC3}	N_u/N_{AISC}	N_u/N_{EWM*}	N_u/N_{DSM}	N_u/N_{DSM}*
Slender sections only	4 Tests + 107 FEM	0.97	0.95	1.02	-	-
Non-slender + slender	10 Tests + 290 FEM	-	-	-	1.06	1.02
	COV:	0.048	0.053	0.035	0.100	0.041